Article | Open Access

Energy Materials

Yan *et al*. *Energy Mater*. **2026**, *6*, 600094 **DOI:**10.20517/energymater.2026.135

A wireless sensor and energy harvesting system based on piezoelectric-electromagnetic synergy in P(VDF-TrFE) films

Yingjuan Yan[1], Weimin Xia[1,*], Lu Wang[2,*], Hong Pan[1], Xiaofang Zhang[1], Yinghui Wang[1], Xinru Wang[1], Ronghao Yang[3]

Keywords: Energy harvester, self-powered, piezoelectric, electromagnetic

Citation: Yan, Y.; Xia, W.; Wang, L.; Pan, H.; Zhang, X.; Wang, Y.; Wang, X.; Yang, R. A wireless sensor and energy harvesting system based on piezoelectric-electromagnetic synergy in P(VDF-TrFE) films. *Energy Mater.* **2026**, *6*, 600094. https://dx.doi.org/10.20517/energymater.2026.135

Received: 25 May 2026
First Decision: 23 Jun 2026
Revised: 9 Jul 2026
Accepted: 23 Jul 2026
Published: 5 Aug 2026

Academic Editor: Yuping Wu
Copy Editor: Fangling Lan
Production Editor: Fangling Lan

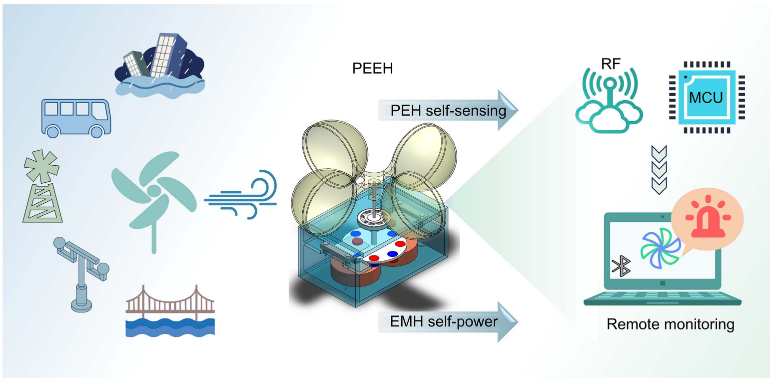

Abstract

With the rapid growth in the number of Internet of Things (IoT) nodes, developing self-powered systems that combine high energy conversion efficiency with stable power supply capabilities has become a key challenge. To address the issues of narrow operating bandwidth, poor environmental adaptability, and limited output power in traditional single-mechanism energy harvesters, this paper proposes a piezoelectric, electromagnetic hybrid energy harvester (PEEH) based on a bidirectional magnetic excitation mechanism. Guided by the finite element method, the rotor's magnetic circuit structure was optimized to create a periodically alternating bidirectional "push-pull" magnetic excitation. This effectively suppresses asymmetric oscillations in the cantilever beam, enabling stable harmonic motion and achieving efficient electromechanical coupling with a β-phase-rich poly(vinylidene fluoride-trifluoroethylene) thin film. Thanks to this synergistic design, the PEEH achieves an output voltage of 112 V at a wind speed of 12 m/s, and its total power reaches 38.5 mW at 17 m/s. By further integrating an adaptive under-voltage lockout power management circuit, a fully self-powered wireless monitoring system was developed

[1]School of Materials Science and Engineering, Xi'an University of Technology, Xi'an 710048, Shaanxi, China.
[2]School of Instrument Science and Technology, Xi'an Jiaotong University, Xi'an 710049, Shaanxi, China.
[3]School of Chemical and Process Engineering, University of Leeds, Leeds LS2 9JT, UK.

*__Correspondence to:__ Dr. Weimin Xia, School of Materials Science and Engineering, Xi'an University of Technology, Xi'an 710048, Shaanxi, China. E-mail: xiaweimin@xaut.edu.cn; Dr. Lu Wang, School of Instrument Science and Technology, Xi'an Jiaotong University, Xi'an 710049, Shaanxi, China. E-mail: wang.lu@xjtu.edu.cn

that enables periodic Bluetooth data transmission even under intermittent wind conditions. This study demonstrates that synergistically enhancing piezoelectric and electromagnetic energy conversion through magnetic circuit optimization can effectively improve wind energy utilization efficiency and system power supply stability, providing an efficient, stable, and grid-independent self-powered solution for next-generation wireless IoT nodes.

INTRODUCTION

With the proliferation of the Internet of Things (IoT) and smart city infrastructures, wireless sensor networks (WSNs) have been widely adopted as the core sensing layer across diverse sectors, including environmental monitoring[1], industrial automation[2], intelligent transportation[3], and healthcare[4]. However, the exponential expansion of these sensor nodes has precipitated a dramatic surge in aggregate energy demand. Traditional battery-reliant power solutions are constrained by finite lifespans, frequent maintenance requirements, and severe environmental pollution, collectively presenting a critical bottleneck to the ubiquitous deployment of WSNs[5]. To circumvent these limitations, environmental energy harvesting technologies[6,7], thermal[8], and solar[9] and convert them into electricity. This paradigm effectively untethers sensing[10], computational[11], and wireless communication modules[12] from grid and battery dependencies. Consequently, the development of self-powered wireless sensor nodes is imperative for ensuring sustainable, maintenance-free operation.

Currently, the transduction of mechanical energy into electricity primarily relies on electromagnetic[13], piezoelectric[14], and triboelectric[15] mechanisms. Within the piezoelectric domain, inorganic materials like quartz[16] and lead zirconate titanate (PZT)[17] exhibit high piezoelectric coefficients and robust electromechanical conversion efficiencies; nevertheless, their inherent brittleness and poor processability severely restrict their integration into flexible or conformal devices. Conversely, polymer-based piezoelectric materials, particularly poly(vinylidene fluoride-trifluoroethylene) (P(VDF-TrFE))[18], offer superior structural flexibility, excellent chemical stability, and the capability to efficiently translate subtle mechanical vibrations or pressure variations into measurable electrical signals. Coupled with its inherent biocompatibility, P(VDF-TrFE) has demonstrated unique advantages in wearable electronics[19] such as electronic skin[20] and health monitoring patches[21], as well as in low-power sensing arrays[22-24]. Compared to traditional PVDF, which requires harsh high-voltage polarization conditions, or relaxor ferroelectric terpolymers (such as PVDF-TrFE-CFE), which exhibit severe signal nonlinearity under dynamic mechanical loading, P(VDF-TrFE) can spontaneously form a high-purity polar β phase through simple thermal annealing and exhibits excellent linear response and fatigue resistance, which is crucial for developing high-precision, self-powered sensing microsystems with simplified manufacturing processes. To enhance the electrical performance of next-generation self-powered applications, modifying PVDF-based polymers through microengineering and nanohybridization has become a hot research topic. Representative work includes loading Ni/$CoFe_2O_4$ nanoparticles onto electrospun PVDF fibers, which significantly enhanced the device's energy output through the charge capture effect[7]. Simultaneously, flexible composites constructed from PVDF-HFP and GCN have successfully extended high-efficiency energy harvesting to multimodal sensing scenarios such as sleep monitoring[25]. Besides, to improve environmental energy utilization efficiency, researchers have also developed various hybrid energy harvesting systems, such as hybrid triboelectric nanogenerators that integrate wind and sound energy collection. By sharing electrode structures and optimizing power management circuits, they achieve collaborative collection and supply of multiple environmental energy sources[26]. These studies fully demonstrate that advanced PVDF-based materials and multi-mechanism coupling strategies are valuable for enhancing energy harvesting performance and expanding self-powered applications. Beyond piezoelectricity, electromagnetic induction remains a prevailing technology for micro-scale wind energy harvesting to sustain wireless sensors[27-31]. While numerous hybrid systems integrating electromagnetic, piezoelectric, and triboelectric mechanisms have been developed[32,33], most of these studies focus on improving energy harvesting efficiency or expanding multi-source energy collection capabilities. The hybrid mechanisms mainly serve the purpose of power supply, rather than active sensing. There is still a lack of systematic research on how to achieve deep integration of efficient energy harvesting and active wind speed sensing in the same device. This conventional physical and systemic bifurcation introduces significant technical hurdles, including impedance mismatch, complex power management circuitry, and bulky system architectures, thereby degrading overall operational efficiency. Specifically, in the realm of wireless wind speed monitoring, the traditional architecture, which necessitates separate modules for anemometry and power generation, severely compromises deployment flexibility. Therefore, by leveraging the synergistic effects of piezoelectric and electromagnetic phenomena[34], this approach combines the high power-generation capacity of electromagnetic structures with the ultra-high sensitivity and fatigue resistance of flexible piezoelectric polymers. At the same time, achieving an integrated design that combines energy harvesting with active wind speed sensing represents an important research direction for the development of a new generation of dual-function, self-powered wind speed sensors.

This study proposes a mechanically synergistic, dual-mode, self-powered wind speed sensing system. A rotor that rotates with the wind serves as a unified excitation source, simultaneously generating electrical signals through electromagnetic induction and a non-contact magnetically driven piezoelectric mechanism. This design achieves efficient mechanical synergy while maintaining electrical decoupling, thereby enabling a quantitative assessment of the performance contributions of each mode. The study employed a solution-casting method to fabricate the piezoelectric layer and established a theoretical model of electromechanical coupling; combined with multiphysics simulation, the magnet array of the electromagnetic module underwent multi-objective optimization. Experiments have shown that the device can produce an output voltage of 112 V at a wind speed of 12 m/s, and its total power reaches 38.5 mW at 17 m/s. Relying on an energy management circuit comprising a 0.1 F capacitor and a voltage regulator, the system successfully powered the microcontroller and the RF front-end. Tests confirmed that the average power consumption of this wireless node was effectively controlled at 11.70 mW, with a relative error in wind speed detection of only ±0.6%. This study fully validated the system's ability to operate stably over the continuous term without an external power source, providing a novel approach to the design of highly integrated, self-powered sensor nodes.

EXPERIMENTAL

Preparation of P (VDF-TrFE) piezoelectric sensor

P(VDF-TrFE) powder (PolyK Technologies, USA) with a molar ratio of 75/25 was mixed with N,N-dimethylformamide (DMF, Tianjin Fuyu Fine Chemicals Co., Ltd., China) solvent. A highly crystalline P(VDF-TrFE) film with a thickness of 0.048 mm was obtained via conventional solution casting at 200 °C followed by annealing at 140 °C. Subsequently, the P(VDF-TrFE) film underwent polarization treatment using a polarization device (RK2674A, made in China) and an oil bath piezoelectric polarization device (HYJH-L/20KV, made in China). All P(VDF-TrFE) piezoelectric films in this study were treated using the same polarization process to eliminate the effect of different polarization conditions on piezoelectric performance. Both sides of the film were metalized using silver nano-ink screen printing, and the final assembly formed a piezoelectric sensor, as shown in Figure 1A.

Assembly process of PEEH

The new piezoelectric-electromagnetic hybrid energy harvester (PEEH) has overall dimensions of 60 × 90 × 40 mm^3 and is encapsulated on both sides with transparent acrylic. It primarily consists of a dual piezoelectric cantilever (PEH), a dual electromagnetic module (EMHs), and a rotating assembly (Supplementary Figure 1 for assembly details). The PEH unit (29 × 20 × 0.1 mm^3) consists of a P(VDF-TrFE) piezoelectric film bonded to a flexible substrate using epoxy resin (Purchased from Zhejiang Lixie

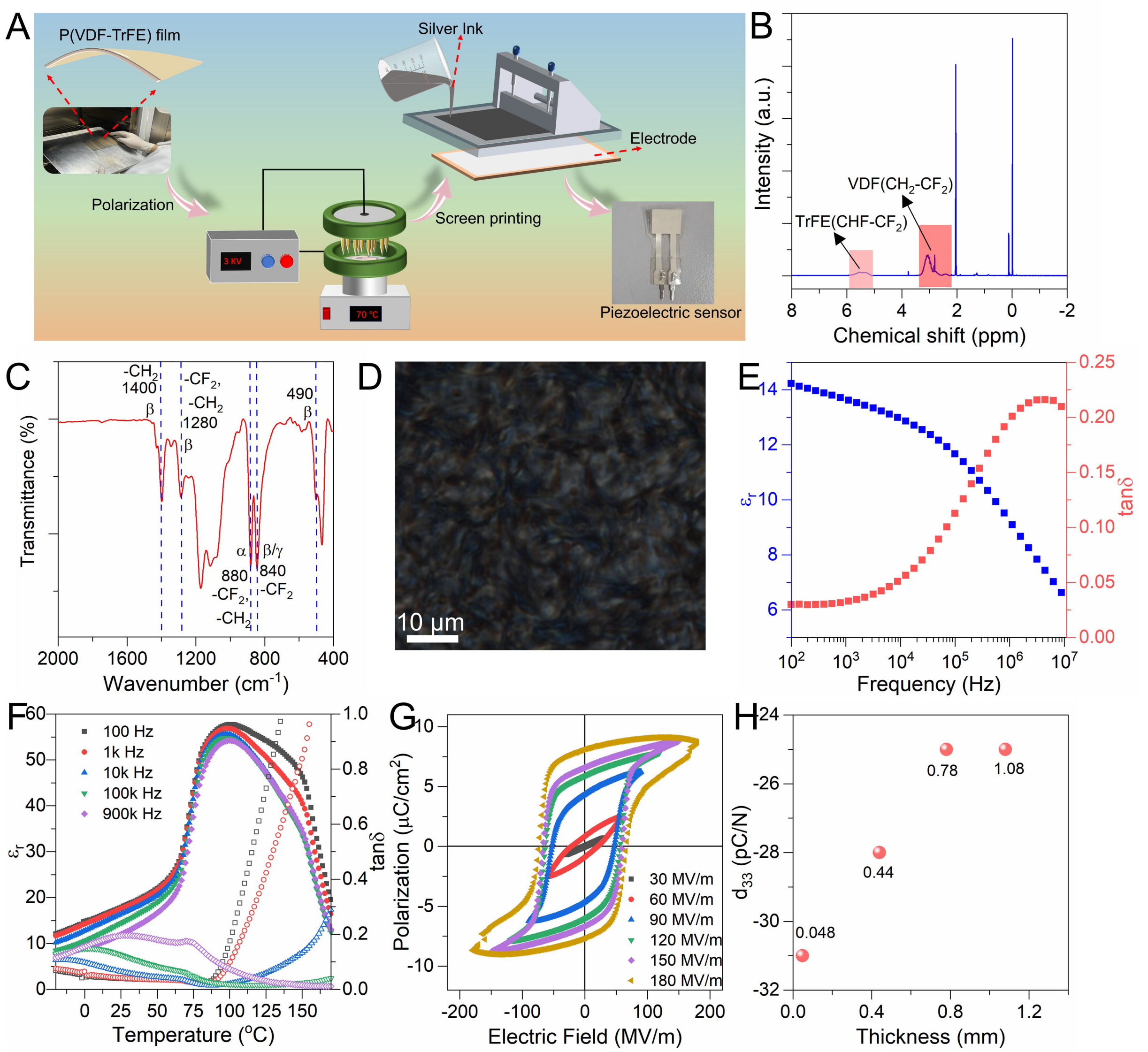

Figure 1. (A) Flowchart for the preparation of piezoelectric sensors, (B) ¹H NMR spectrum of H-P(VDF-TrFE), (C) FTIR spectrum and (D) POM of P(VDF-TrFE) film, (E) Frequency-dependent dielectric properties of P(VDF-TrFE) film, (F) Dielectric temperature spectrum of P(VDF-TrFE) film in the 100 Hz-900 k Hz frequency range and (G) P-E loop, (H) Quasi-static piezoelectric constants of P(VDF-TrFE) films with different thicknesses.

Instrument & Equipment Co., Ltd., China), with a cylindrical magnet (Φ8 × 3 mm) attached to the top of its free end. The EMH module consists of a copper coil (inner and outer diameters of 8 and 36 mm, respectively, and a height of 7 mm) mounted on an acrylic plate. Additionally, the rotating assembly includes an external bell housing, a top sealing plate, and a suspension chassis embedded with eight cylindrical permanent magnets and connected via bearings.

Characterization

1H Nuclear Magnetic Resonance spectroscopy (NMR) spectra were recorded on a Bruker Avance II 400 MHz NMR spectrometer (Bruker, Germany) using C_3D_6O (99.9%, Aladdin) as the solvent. Crystal structure characterization was performed on a Rigaku D/MAX-2400 X-ray diffractometer (XRD, Cu Kα, λ = 0.15406 nm, 40 kV) in Japan. Fourier transform infrared (FTIR) spectra were recorded on a Shimadzu 8400S FTIR spectrometer (400-2,000 cm^{-1}, 4 cm^{-1} resolution). Thermal properties were tested on a Netzsch differential scanning calorimetry (DSC) 214 Polyma differential scanning calorimeter (N_2 atmosphere, 10 °C

min^{-1} heating/cooling rate). Surface morphology was observed and photographed using a Nikon LV100POL polarizing microscope (POM, crossed polarization mode, ×200 magnification). Polarization treatment was performed in a Chinese Huayuan HYJH-L/20 kV oil-bath high-voltage polarizer. Dielectric temperature and frequency spectra were measured using an American Agilent 4284A precision impedance analyzer (100 Hz-10 MHz, AC amplitude 100 mV) coupled with a Linkam THMS600 temperature controller. The ferroelectric loop recordings were obtained using the TF Analyzer 2000 ferroelectric testing system (frequency: 10 Hz) from the German company aixACCT. The piezoelectric constant d_{33} was measured within 24 h after polarization using a ZJ-3 quasi-static d_{33} tester (0.25 N, 110 Hz) from the Institute of Acoustics, Chinese Academy of Sciences.

In this study, ANSYS and Ansoft Maxwell software were used to perform simulation analyses on the piezoelectric cantilever beam and the electromagnetic module, respectively. A finite element simulation analysis of a piezoelectric cantilever beam was performed using ANSYS software. The geometric model was constructed using DesignModeler, a modeling tool within ANSYS. ANSYS software's Adaptive Mesh Refinement was used. During the calculation, the software automatically refines the mesh in key areas based on the magnetic field gradient and stops iterating once preset convergence criteria are met to ensure stable results. The fixed end was set as a fully constrained fixed support, while the forces between the magnets at the free end were applied through fluid-structure interaction or discrete dynamics. The fixed end was configured as a fully constrained fixed support, while the forces between the magnets at the free end were applied using fluid-structure interaction or discrete dynamics. The electromagnetic module was simulated using Ansoft Maxwell software, employing the 3D Transient Solver to accurately simulate the time-dependent changes in magnetic flux during rotor rotation. The boundary of the external air domain was set to “Radiation” to simulate an infinite space, while the coil was configured as “Winding excitation” with the actual number of turns and internal resistance defined. A rotating motion band was established around the rotor assembly, with the rotational speed strictly matched to the rotational speed under the wind speed conditions of the experimental test.

To characterize the output characteristics of the energy harvester, a dedicated vibration and wind tunnel testing platform was constructed [Supplementary Figure 2]. The vibration platform consists of a controller (Yiheng), a power amplifier (SA-PA080, Wuxi Shiao Technology Co., Ltd., China), a shaker, and an accelerometer (EV4200) to provide and monitor the reference vibration excitation; The wind tunnel platform combines a low-noise axial flow wind tunnel (for low wind speeds) with an axial flow fan (for high wind speeds), and is equipped with an anemometer (GM8910, Shenzhen BENETECH Biaozhi Instruments, China) and tachometer (Xima AR925 Contact-Type Tachometer, Xima Instruments SMART SENSOR, China) to monitor the flow field and prototype rotational speed in real time. Additionally, the electrical testing platform [Supplementary Figure 3] uses a digital oscilloscope (RIGOL DS1054Z, Shenzhen Huaqing Instrument Co., Ltd., China) and an electrometer (Keithley-6482, China) to measure and record the device’s output voltage and short-circuit current, respectively.

RESULTS AND DISCUSSION

Film structure and properties

The chemical structure of the synthesized P(VDF-TrFE) copolymer was first corroborated using ^{1}H NMR spectroscopy [Figure 1B]. The multiplet observed at 2.2-3.3 ppm is assigned to the protons in the -CH_2-CF_2- groups of the VDF units, while the signal spanning 5.1-6.0 ppm corresponds to the -CHF-CF_2- groups of the TrFE units, accurately reflecting the expected monomeric configuration. Crystallographic analysis via XRD [Supplementary Figure 4] reveals a single, sharp (200/110) diffraction peak at 2θ = 20.9°. The complete absence of α-phase characteristic peaks indicates that the film crystallizes almost exclusively into the electroactive β phase, establishing a robust structural foundation for its high-voltage electrical response. This high β phase purity is further substantiated by FTIR spectroscopy [Figure 1C]. Characteristic vibrational bands of the β phase are prominent at 490, 840, 1,280, and 1,400 cm^{-1}, whereas the 880 cm^{-1} band, which is indicative of the nonpolar α phase, is nearly absent[35]. This result confirms the overwhelming dominance of the polar β conformation.

Thermal and morphological evaluations further validate the film's quality. DSC [Supplementary Figure 5] demonstrates a Curie temperature (T_c) of 98 °C and a melting point (T_m) of 156 °C. These values align with literature reports for highly crystalline P(VDF-TrFE), ensuring adequate thermal stability across the anticipated device operating temperature range. Macroscopically, this high crystalline quality is reflected in the polarized optical micrograph [Figure 1D and Supplementary Figure 6], which exhibits a typical lamellar grain morphology characterized by radially symmetric light-dark extinction bands, a hallmark of ordered lamellar crystal stacking.

The electrical properties, which are pivotal for electromechanical coupling, were systematically characterized. At room temperature and 100 Hz, the film exhibits a relative dielectric constant (ε_r) of approximately 14 and a low dielectric loss (tanδ < 0.04) [Figure 1E]. It is noteworthy that the pure P(VDF-TrFE) film exhibits a relatively high dielectric loss (~ 0.2) at 10^7 Hz, which is inherently governed by the unavoidable intrinsic dipole relaxation of the polar polymer under ultra-high frequency electric fields, consistent with the standard physical characteristics of P(VDF-TrFE) films[36,37]. As the frequency increases, ε_r monotonically decreases while tanδ slightly increases, a behavior entirely consistent with the classical dipole orientation polarization model. Moreover, the temperature-dependent dielectric spectrum [Figure 1F] displays a pronounced dielectric peak at T_c, capturing the classic ferroelectric-to-paraelectric phase transition. The intrinsic ferroelectricity of the film is explicitly verified by the polarization-electric field (P-E) hysteresis loop [Figure 1G]. Under an applied electric field of 180 MV/m, the remnant polarization (P_r) reaches 8.1 μC cm^{-2} with a coercive field (E_c) of 67 MV/m, underscoring the film's robust dielectric strength and excellent polarization switching capability. Finally, the longitudinal piezoelectric coefficient (d_{33}) exhibits an initial decrease before stabilizing as a function of increasing film thickness [Figure 1H]. Notably, at an optimized thickness of 48 μm, the d_{33} value peaks at -31 pC/N, representing the upper echelon of performance for flexible polymer piezoelectric. This superior electromechanical coupling directly empowers the high-sensitivity, self-powered sensing capabilities essential for subsequent microelectromechanical systems (MEMS) applications, particularly in wind speed monitoring and hybrid energy harvesting.

Structural design and working principle

Building upon the aforementioned material advantages, this study proposes a novel PEEH specifically engineered for the concurrent extraction of ambient wind energy and the autonomous monitoring of wind speed. Figure 2A delineates the architectural flowchart of the PEEH-enabled wireless sensor node, which integrates four fundamental modules: the electromechanical structure, power management, signal processing, and wireless transmission. Operationally, ambient wind kinetic energy is simultaneously scavenged by the electromagnetic harvester (EMH) and the piezoelectric harvester (PEH). Crucially, the system intelligently bifurcates these harvested outputs based on their optimal functions. The EMH, comprising dual stationary coils, serves as the primary power generator. The induced alternating current (AC) is routed through a comprehensive power management circuit (PMC), which includes a rectifier, an undervoltage lockout (UVLO) mechanism, storage capacitors, and a voltage regulator to provide a stable, regulated direct current (DC) to the microcontroller unit (MCU). Conversely, the two well-designed P(VDF-TrFE) PEHs function as self-powered active sensors, directly correlating wind speed with their oscillatory output frequency. By integrating these power supply and sensing pathways, the MCU accurately processes the frequency signals and transmits the wind data via a radio frequency (RF) module. This highly integrated paradigm eliminates the reliance on wired power grids or frequent battery replacements, offering a robust,

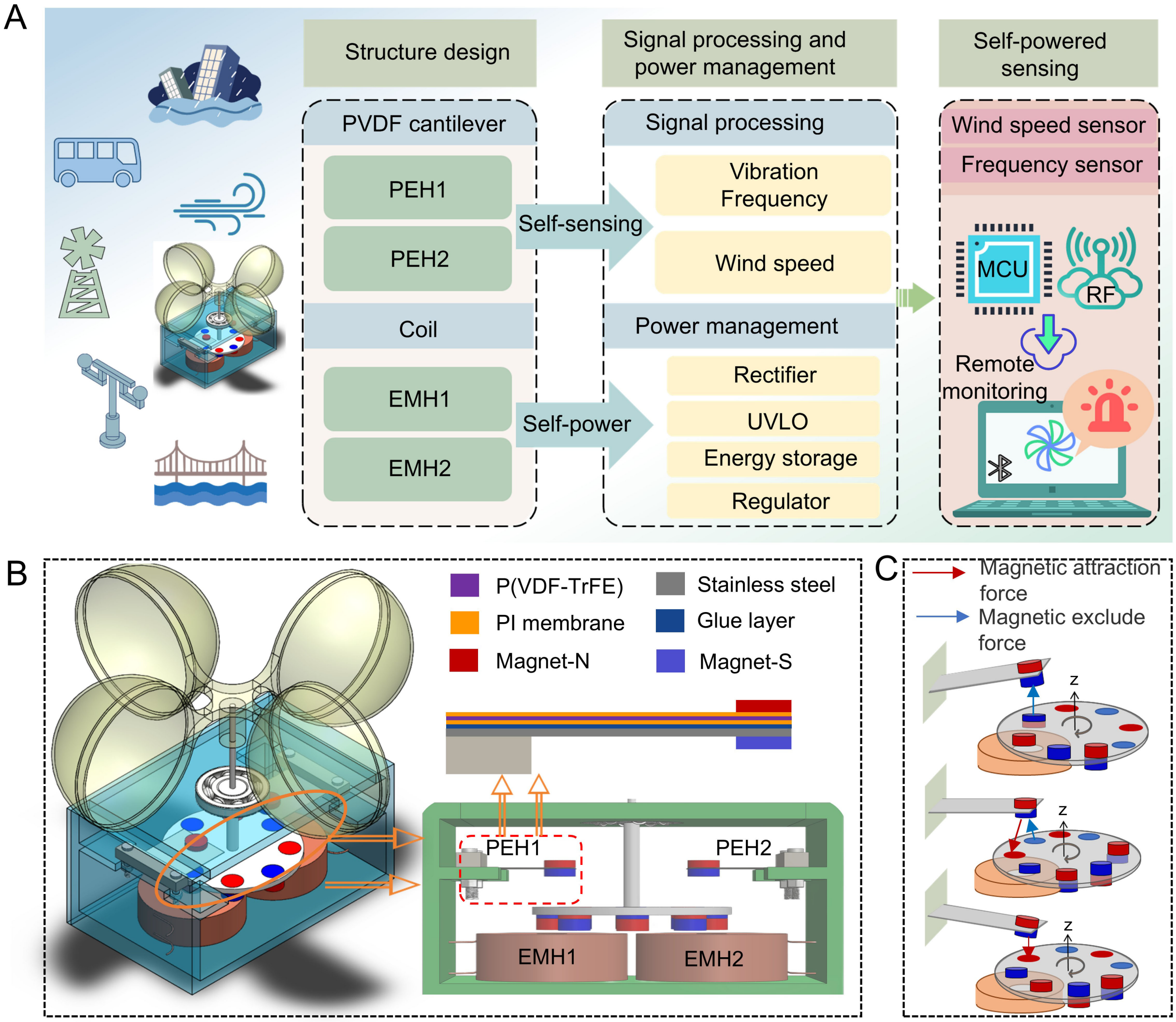

Figure 2. (A) Structural design flowchart of PEEH, (B) Schematic diagram of the structure of PEEH, (C) Schematic diagram of the vibration principle of PEH.

maintenance-free monitoring solution ideal for remote deployments, such as meteorological stations, bridges, and communication towers.

The structural configuration that actualizes these dual functions is detailed in Figure 2B. The EMH module features coils symmetrically anchored to a stationary base, concentrically aligned with the trajectory of the rotor magnets to maximize magnetic flux linkage. To enhance the system's responsiveness and reliability under low-wind conditions, the rotor disk incorporates an opposing magnetic suspension mechanism; these symmetrically positioned reverse magnets effectively minimize mechanical friction and starting torque. As the wind-driven rotor assembly spins, the cylindrical magnets attached to its periphery sweep across the stationary coils, inducing an electromotive force for efficient bulk energy harvesting. Concurrently, this rotational motion actuates the piezoelectric sensing module. As illustrated in Figure 2C, periodic alternating magnetic attraction and repulsion forces occur between the suspended magnets on the rotating disk and the permanent magnets affixed to the free ends of the PEH cantilevers. This non-contact magnetic plucking mechanism drives the PEH into sustained mechanical oscillation. Consequently, variations in ambient wind speed are precisely translated into proportional rotor speeds, which in turn dictate the excitation frequency and voltage response of the PEH. This elegantly coupled mechanical design ensures that dynamic wind variations are faithfully captured as electrical signals, thereby establishing a highly reliable foundation for self-powered sensing.

Simulation analysis of PEEH

Finite element method (FEM) simulations were utilized to optimize the structural design, evaluate mechanical stability, and maximize the overall energy conversion efficiency of the PEEH. FEM simulations were mainly used to guide rotor structure design and to compare the relative differences in magnetic field distribution and magnetic excitation characteristics under different magnet configurations, based on which the optimal structure for subsequent experiments was selected. Initially, modal analysis was performed on the PEH cantilever. As illustrated in Supplementary Figure 7, the simulations revealed three distinct vibration modes: the fundamental bending mode, a symmetrically balanced mode, and a higher-order node-splitting mode. Notably, the fundamental (first-order) mode exhibits a relatively low resonant frequency of 56.75 Hz. This low-frequency characteristic ensures that the cantilever is highly responsive and can be readily excited by the low-frequency, small-amplitude mechanical stimuli generated by the wind-driven rotor, providing a robust mechanical foundation for subsequent energy harvesting.

Beyond structural dynamics, the configuration of the rotor significantly dictates the overall electromechanical performance of the system[38]. Consequently, we systematically investigated the influence of the rotor's permanent magnet array-specifically the magnet count and spatial arrangement-on both electromagnetic induction and piezoelectric excitation. As depicted in Figure 3A, three configurations were modeled: six uniformly distributed magnets with identical polarities (Model A), six magnets with alternating polarities (Model B), and eight magnets with alternating polarities (Model C). The vector spatial distributions of the magnetic flux density for each configuration were examined [Figure 3B and Supplementary Figure 8]. FEM simulation results show that among the three studied rotor magnet configurations, Model C generates the highest magnetic flux density. This enhanced magnetic field helps improve electromagnetic induction, so Model C was chosen as the rotor structure for subsequent device fabrication and electrical performance testing.

To better understand how different rotor structures affect the piezoelectric excitation methods, we conducted a FEM analysis of the instantaneous magnetic forces on the free-end magnet of the PEH along the Y and Z axes at 350 rpm, to compare the magnetic excitation characteristics produced by different magnet configurations [Figure 3C]. Under Models A and B, the PEH tip experiences a continuously positive (unidirectional) magnetic force in the Z direction, imposing a static upward deflection on the cantilever that results in restricted oscillation and an irregular, asymmetric voltage output. In stark contrast, Model C subjects the PEH tip to strictly alternating positive and negative magnetic forces (a bidirectional "push-pull" effect). FEM shows that Model C generates periodic alternating magnetic excitation characteristics, which theoretically makes it better at driving the piezoelectric cantilever to form stable back-and-forth vibrations, providing a reasonable explanation for getting more stable piezoelectric output. Furthermore, piezoelectric potential simulations [Figure 3D] indicate that the generated voltage reaches its maximum near the fixed clamped end of the cantilever, which is entirely consistent with the classical mechanical stress distribution of a cantilever beam. Compared to the other configurations, Model C induces the largest deformation amplitude and, consequently, the highest voltage output. In summary, the sophisticated rotor architecture of Model C comprehensively optimizes energy harvesting efficiency while simultaneously enhancing signal fidelity. Therefore, this study chose Model C, which had the best performance in this work, for further device fabrication and electrical performance testing.

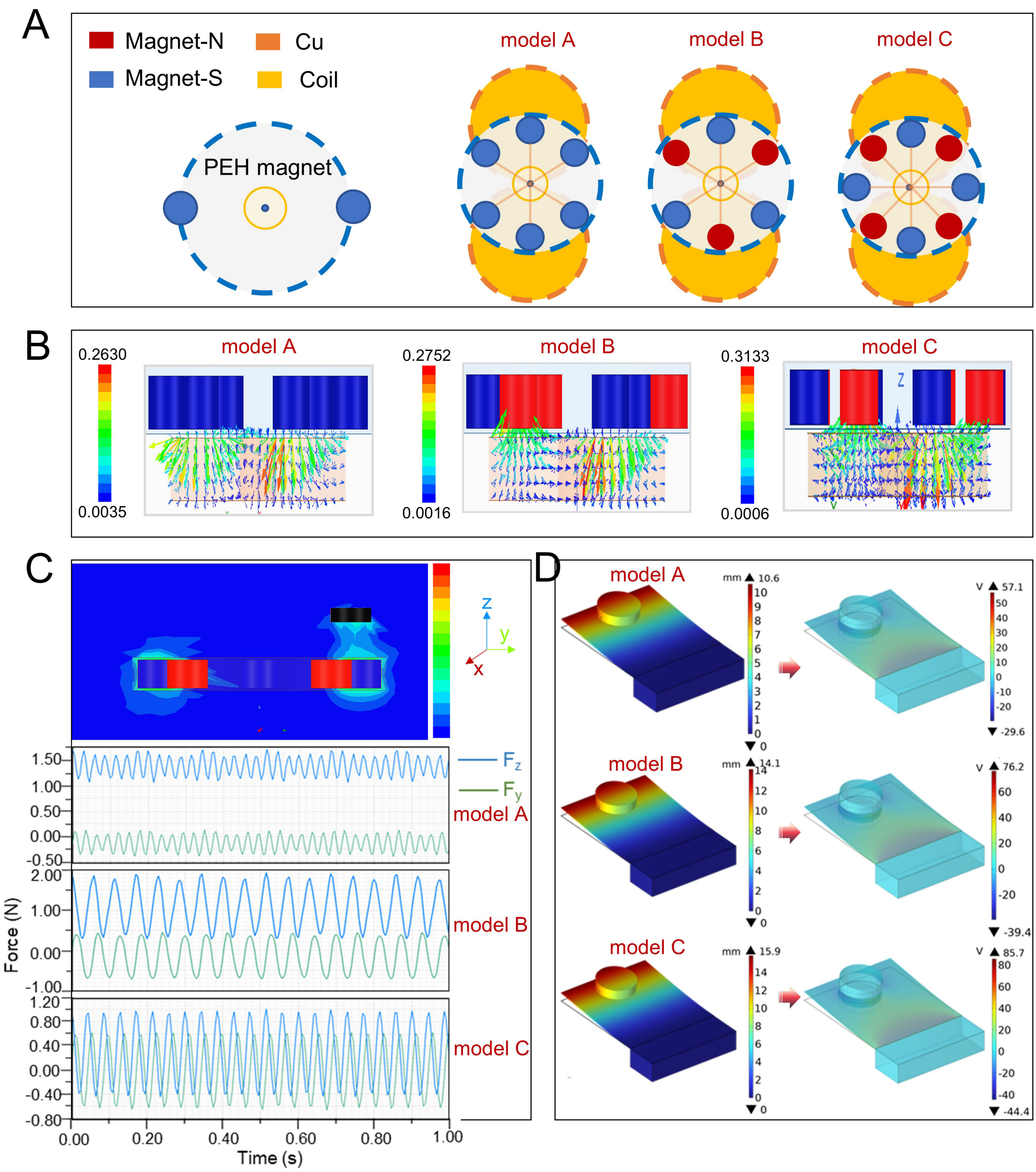

Figure 3. (A) Schematic of the model simulation in three different modes, (B) Simulation of the coil magnetic field distribution in three different modes, (C) Simulation of the electromagnetic force in z- and y-directions in three different modes, (D) Amplitude response and voltage response of the PEH in different modes.

Electrical properties of PEEH

Guided by the preceding simulation results, the rotor configuration of Model C, which ensures optimal energy-harvesting efficiency and highly uniform piezoelectric excitation, was selected for fabrication and experimental validation. Initially, to assess the system's dynamic characteristics and its resilience to external environmental vibrations, frequency sweep experiments were conducted to determine the actual resonant frequency of the PEH cantilever. As illustrated in Supplementary Figure 9, frequency sweeps (45-65 Hz) under varying base accelerations experimentally confirm a resonant peak at ~56 Hz. This result aligns

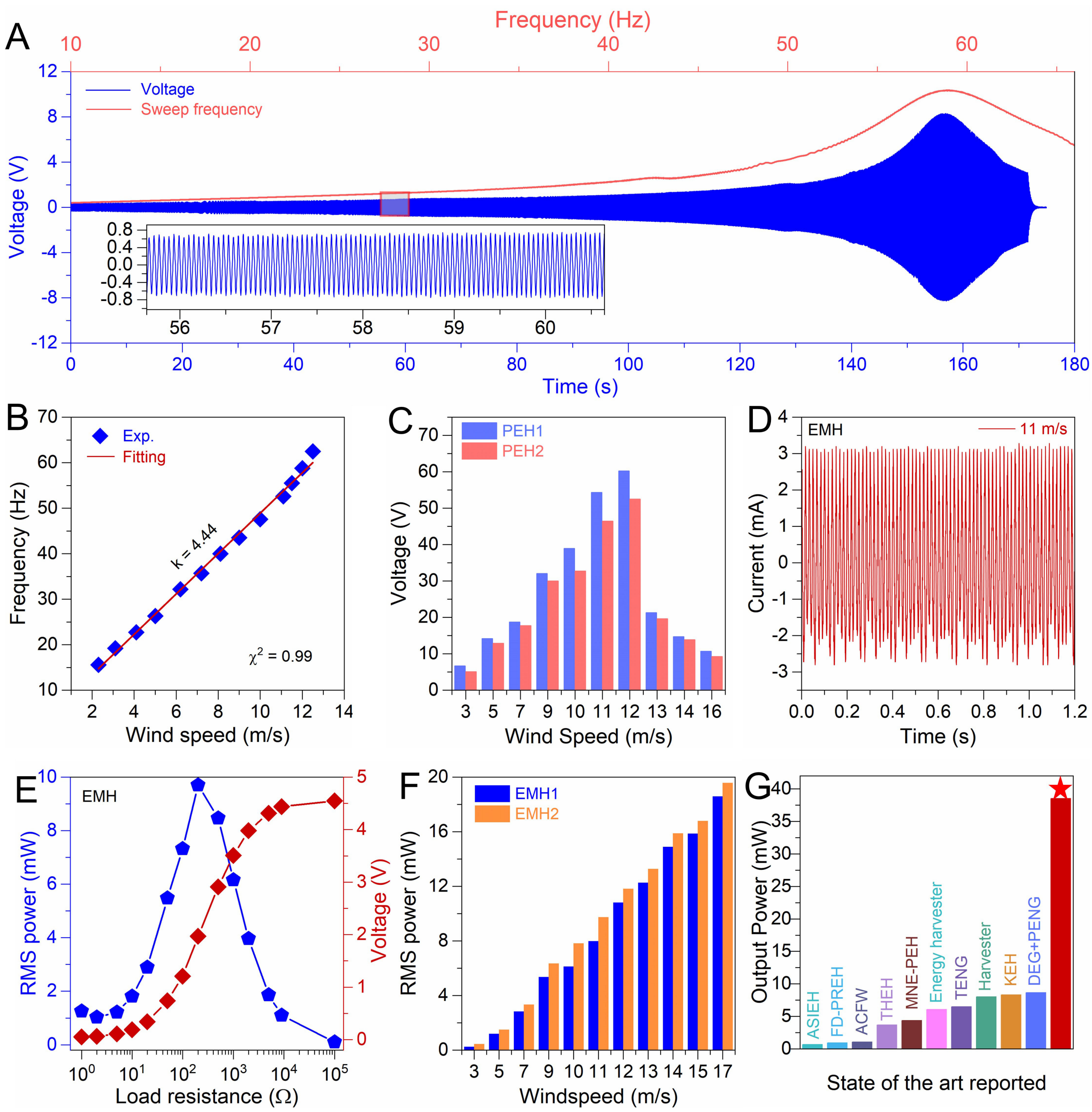

Figure 4. (A) Voltage output and swept voltage output response of PEH at 3.5 m/s wind speed, the illustration shows the amplified output of the sweep voltage within the 55-60 s range (Frequency:10-70 Hz), (B) Fitting of the relationship between wind speed and vibration frequency of PEH, (C) Voltage response of PEH at different wind speeds, (D) Current response of EMH at constant wind speed, (E) Output power and output voltage response of EMH at different load resistances at 12 m/s wind speed, (F) Output power of EMH at different wind speeds, (G) Comparison chart of PEEH output power with other literature reports.

excellently with our theoretical modal analysis. To further isolate the vibration characteristics and evaluate the system's robustness against external mechanical crosstalk, the permanent magnet at the free end of the PEH was substituted with a non-magnetic copper disc of equivalent mass [Figure 4A]. A continuous frequency sweep (10-70 Hz at an acceleration of 9.8 m/s^2) was applied to the base while maintaining a constant wind speed of 3.5 m/s. The results demonstrate that the overall voltage response is a direct superposition of the wind-induced excitation and the external base vibration. Crucially, once the external frequency sweep was terminated, the PEH immediately returned to its stable baseline output driven solely by the wind. These findings conclusively demonstrate that external environmental vibrations do not disrupt the fundamental electromechanical coupling of the PEEH, thereby guaranteeing robust operational stability in complex, real-world deployment scenarios.

Subsequently, the electromechanical performance of the fully assembled PEEH system was systematically evaluated across a broad spectrum of wind conditions [Supplementary Figure 10]. Figure 4B confirms its core sensing capability. The figure presents the frequency–wind speed linear response analysis of the PEH within the range of 2-13 m/s, demonstrating a strong linear correlation between the output oscillation frequency of the PEH and the ambient wind speed. This strict linearity confirms the PEH's exceptional sensitivity and reliability, establishing it as an ideal active wind speed sensor. Detailed analyses of the output voltage further elucidate the dynamic behaviors of both modules. As depicted in Figure 4C and Supplementary Figure 11, as the rotor-induced excitation frequency approaches the mechanical resonance frequency of the cantilever (~56 Hz), the PEH voltage initially increases with wind speed, reaching a total output of 112 V at 12 m/s. However, once the wind speed drives the excitation frequency beyond the resonance threshold, the output voltage generated by the cantilever's vibration amplitude will naturally decay. In contrast, governed by Faraday's law of electromagnetic induction, the output voltage of the EMH exhibits a continuous linear increase with wind speed [Supplementary Figure 12]. Short-circuit current measurements conducted at a reference wind speed of 11 m/s [Figure 4D and Supplementary Figure 13] confirmed that both modules produced stable and continuous current output. To maximize energy extraction, impedance matching tests were performed at a wind speed of 12 m/s [Figure 4E and Supplementary Figure 14], yielding optimal load values of 2 MΩ for the PEH and 200 Ω for the EMH, respectively. Notably, the effective operational range of the proposed hybrid energy harvester extends to 3-17 m/s, within which stable electrical outputs can be generated. When connected to a 200 Ω load, Figure 4F shows the EMH's best output power at different wind speeds in the 3-17 m/s range. At 17 m/s, the EMH's total output power reaches as high as 38.5 mW. Finally, the superior power generation capability of the proposed PEEH is further contextualized in Figure 4G, where it demonstrates a significant competitive advantage over other recently reported piezoelectric and hybrid energy harvesters[30,39-47]. In summary, the synergistic integration of the PEH and EMH affords highly accurate wind sensing alongside continuous, high-efficiency energy harvesting, flawlessly fulfilling the power requirements of autonomous wireless sensor nodes.

Energy harvesting circuit

To efficiently convert the harvested AC energy into a continuous and stable DC power supply for the wireless sensor node, a dedicated power management circuit (PMC) was engineered. Initial evaluations of the electromagnetic modules (EMH1 and EMH2) at a wind speed of 4.5 m/s [Figure 5A and B] reveal that connecting the EMH outputs in series prior to rectification yields the optimal electrical output. Taking into account the forward voltage drop of approximately 0.3 V across the rectifier diode, the 4.2 V input voltage yields a regulated DC output of approximately 3.9 V after rectification, corresponding to a rectification efficiency of approximately 92.86% (Figure 5C for the schematic diagram). At the heart of the PMC is the BQ25570 power management integrated circuit, which integrates an MPPT algorithm and a buck-boost energy management module to efficiently charge the supercapacitor. According to the BQ25570 data sheet, the converter achieves a conversion efficiency of approximately 80% under typical operating conditions. Therefore, the overall energy conversion efficiency of the PMC can be estimated based on the rectification efficiency and the BQ25570 conversion efficiency, which is approximately 74.3%. Then, various energy storage components were used to evaluate the charging dynamics under different wind speeds [Figure 5D]. At a wind speed of 4.5 m/s, capacitors with capacities of 1,000 and 2,200 μF both reached about 3 V within 100 s. And as the wind speed increased to 7 m/s, the charging voltage for both capacitors went up to around 6.0-6.5 V. Notably, at an elevated wind speed of 11 m/s, the system demonstrated exceptional charging capability, rapidly charging a substantial 0.1 F supercapacitor to 4 V in merely 275 s [Figure 5E]. The experimental test bench and the comprehensive PMC topology are provided in Figure 5F and Supplementary Figure 15, respectively.

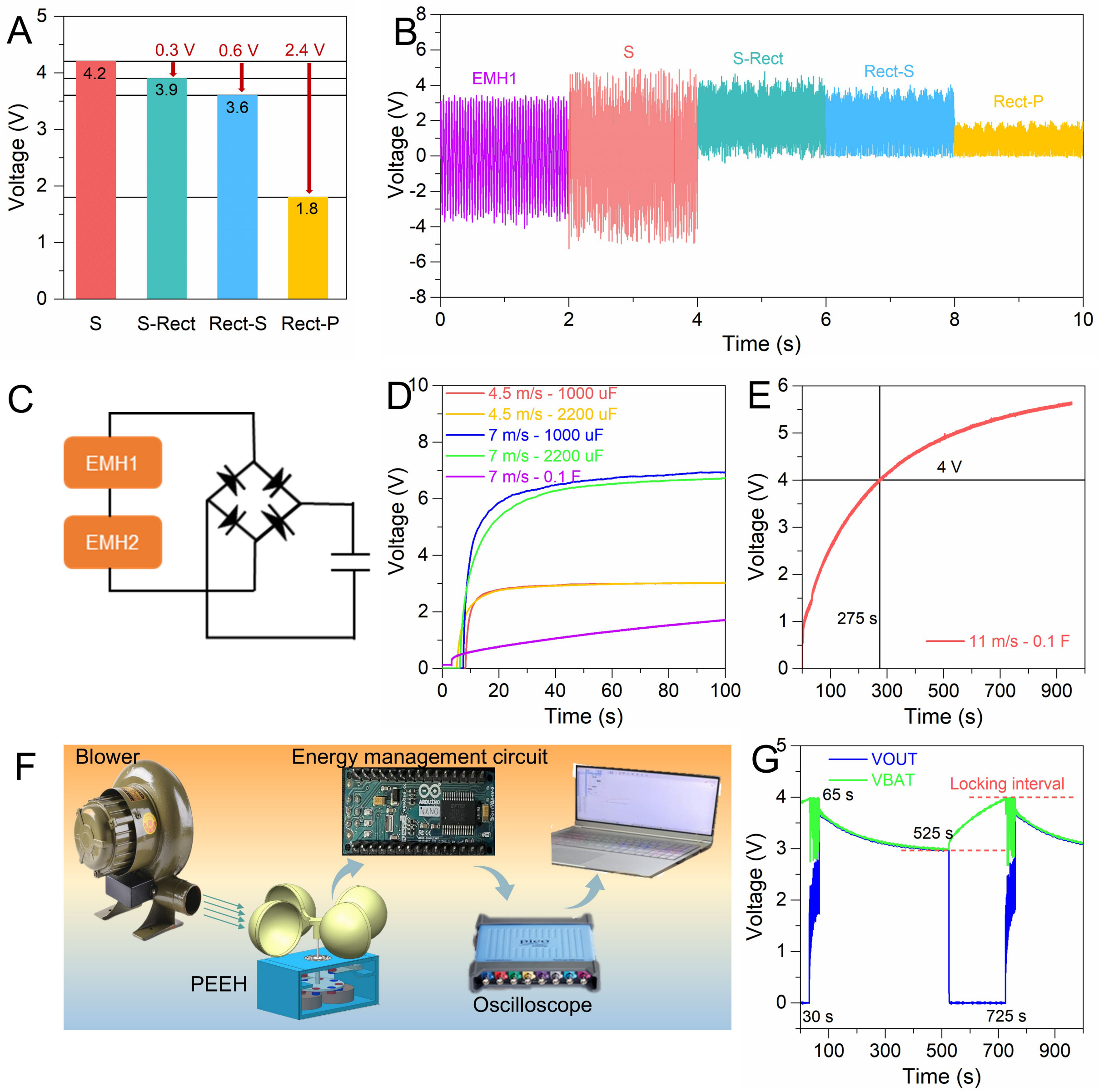

Figure 5. (A amd B) Outputs of EMH1 and EMH2 with different connections to the rectifier circuit (S: denotes the output voltage of the two coils in series, S-Rect: denotes the output voltage of the two coils in series and then rectified, Rect-S: means it first goes through a rectifier circuit to convert to DC output, and then combines in a series connection structure, and Rect-P denotes the output voltage of the two coils rectified and then in parallel), (C) Rectifier module circuit diagram, (D) Charging curves of PEEH for different capacitors, (E) Charging curves of PEEH for 0.1 F supercapacitor at 11 m/s wind speed, (F) energy management circuit test, (G) Circuit output test at 11 m/s wind speed.

To ensure the uninterrupted operation of the sensing node, the system employs strict hysteresis voltage threshold management utilizing the IC's UVLO feature. Regulated power delivery is triggered only when the supercapacitor voltage reaches an upper threshold of 4.0 V, and is suspended to initiate recharging when the voltage drops to a lower limit of 3.0 V. This autonomous management is experimentally validated by the continuous voltage waveform recorded at 11 m/s [Figure 5G]. Following an initial 275 s charging phase to 4.0 V, the PMC delivers a strictly regulated 3.6 V to the load. Once continuous discharge depletes the capacitor to 3.0 V, the UVLO mechanism seamlessly isolates the load, allowing the supercapacitor to recharge. A full charging and energy recovery cycle takes about 11.6 min, with the system providing continuous power for around 7.7 min. In conclusion, the intelligently managed PEEH system demonstrates exceptionally reliable operation across a broad spectrum of wind conditions. By autonomously managing the charging and discharging cycles, it provides a highly practical, maintenance-free power foundation tailored for self-powered wireless sensor nodes deployed in remote engineering infrastructures, such as bridges and communication towers.

Self-powered wind speed sensor

To enable autonomous operation of wireless sensor nodes, we introduce a parallel resistor to adjust and stabilize the output voltage by connecting a 20 kΩ resistor [Figure 6A]. This configuration clamps the output voltage within the safe operating range of the MCU. The system integrates a CC2340 bluetooth low energy (BLE) module to minimize overall energy consumption. Initial power profiling revealed that, under a 3.6 V supply in a continuous active mode, the MCU and BLE module draw an average current of 8.14 mA, equating to a power consumption of 29.30 mW [Figure 6B]. Recognizing that this continuous draw exceeds the steady-state generating capacity of the PEEH, we implemented an event-driven duty-cycling power management strategy. Specifically, the sensor node operates on a 24 s periodic cycle, wherein the energy-intensive BLE module is briefly awakened solely during the active phase for data acquisition and wireless transmission [Figure 6C]. This optimized time-division approach drastically reduces the system's average current to 3.25 mA (lowering power consumption to 11.70 mW), successfully aligning the load demand with the PEEH's energy harvesting capacity and enabling sustained self-powered operation.

Having secured the system's power budget, the operational endurance and reliability of the complete PEEH were systematically evaluated. To simulate harsh continuous outdoor environments, the system was subjected to a high-speed (17 m/s) endurance test for 30 min [Figure 6D]. Throughout this rigorous monitoring period, the PEEH maintained a highly stable voltage output with no observable mechanical degradation or electrical performance fluctuations, substantiating its robust durability for long-term engineering deployments. Furthermore, the system's start capability under suboptimal conditions was verified. As depicted in Figure 6E, even under a gentle breeze of 4.5 m/s, the power management circuit successfully accumulated sufficient energy over 1,700 s to reach the 4.0 V threshold, thereby triggering the regulated VOUT to awaken the sensor node. This confirms the circuit's exceptional practicality and resilience in low-wind-speed scenarios.

Finally, the core function of PEEH, namely accurate wind speed monitoring, was evaluated. By extracting wind speed data from the vibration frequency of the P(VDF-TrFE) cantilever, the system exhibits inherent immunity to the voltage amplitude attenuation that plagues traditional amplitude-based measurement methods. Field validations [Figure 6F and Supplementary Figure 16] demonstrated that at a reference wind speed of 6.5 m/s, the oscilloscope-measured baseline vibration frequency was 33.22 Hz. The system’s wireless transmission and detected frequencies were 33.25, 33.57, and 33.37 Hz, respectively, with a maximum frequency error of only 1.05%. This error was primarily due to the uncertainty of the MCU clock reference and hardware noise in the signal conditioning circuit. Accordingly, the maximum relative error of the calculated wind speeds (6.47, 6.54, and 6.50 m/s) was extremely low, at only 0.6%. This is attributable to the rigorous calibration of high-precision commercial anemometers, the system algorithm’s effective filtering of random hardware noise through multi-point averaging, and the mathematical convergence of the calibration formula within the current wind speed range, thereby achieving wind speed measurement accuracy superior to that of frequency-based measurements. Subsequent synchronous benchmarking against a commercial standard anemometer (GM8910) confirmed that the device maintains an overall measurement error of ≤ 1.05% across a broad wind speed range of 3-17 m/s, fully satisfying the stringent accuracy requirements for engineering measurements. These compelling results conclusively demonstrate that the PEEH successfully unites stable, reliable energy harvesting with high-precision sensing, offering a highly viable hardware foundation for self-powered wireless IoT networks. This work verifies the device’s performance under

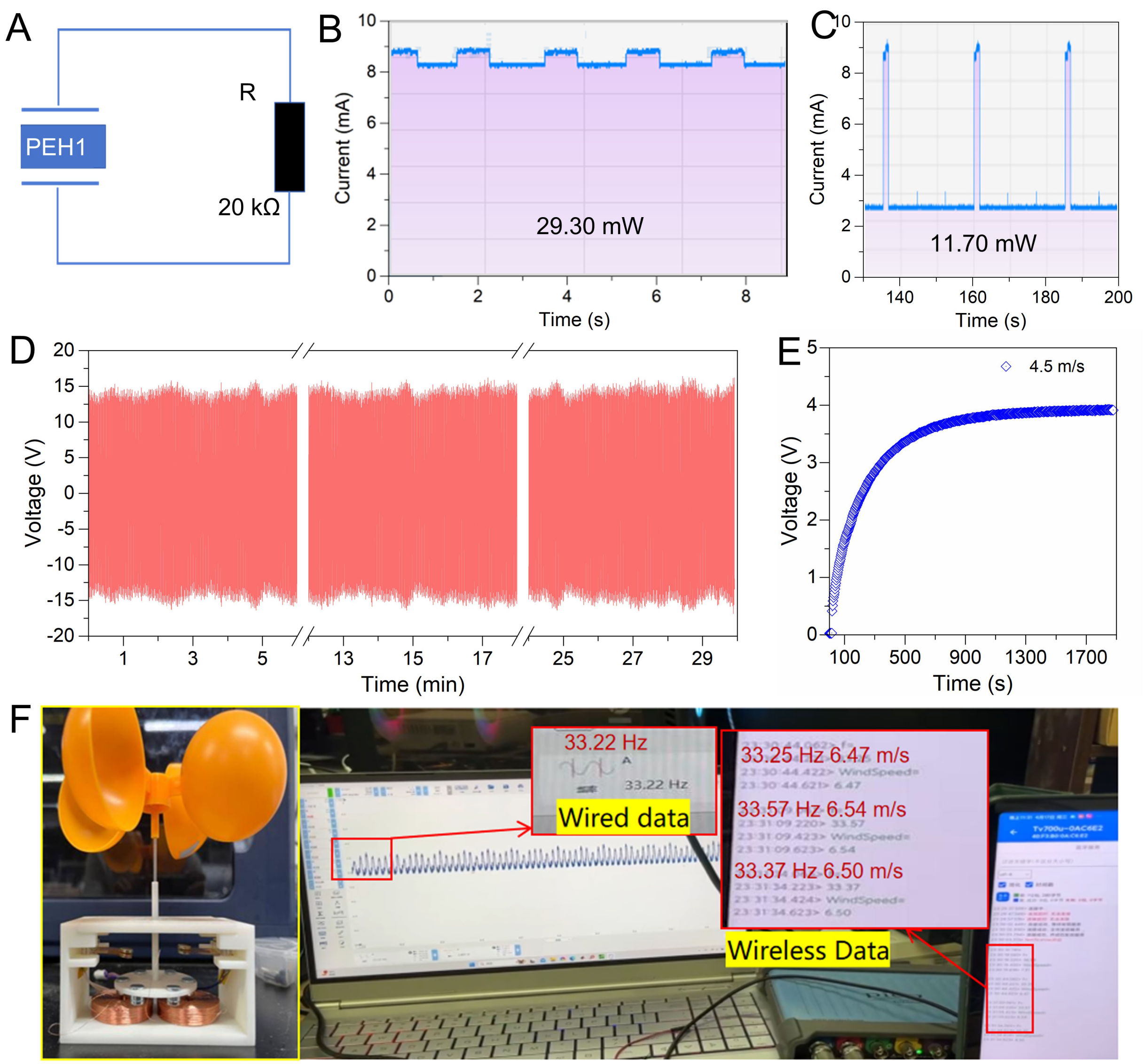

Figure 6. (A) Bucking circuit diagram, (B) Normal operating and (C) Low power consumption power curve of the WSN, (D) Endurance test of the PEEH at 17 m/s, (E) Weak wind start test of the PEEH at 4.5 m/s, (F) PEEH wireless sensor system validation.

laboratory conditions, and future work will further test it in outdoor environments and evaluate continuous operational stability to promote its practical engineering applications.

CONCLUSIONS

This study successfully develops a highly integrated PEEH to enable a fully self-powered, wireless wind speed sensing node. The architecture is fundamentally grounded in the superior material properties of a synthesized P(VDF-TrFE) film, capitalizing on its high β-phase purity, robust piezoelectric coefficient, and broad thermal stability. At the structural level, comprehensive multiphysics simulations were employed to optimize the magnetic rotor array, seamlessly unifying efficient electromagnetic induction with stable, harmonic piezoelectric excitation. Experimental evaluations show that the PEH and EMH modules can output a total voltage of 112 V and a total power of 38.5 mW, respectively. Facilitated by a tailored power management circuit, the system can rapidly charge a substantial 0.1 F supercapacitor to 4.0 V in merely 275 s, robustly satisfying the energy demands of the autonomous node. System-level integrations, coupled with an intelligent, event-driven duty-cycling strategy, enable highly accurate wind speed monitoring across a broad operating range of 3-17 m/s, exhibiting a minimal frequency measurement error of ≤ 1.05%. Furthermore, the device exhibited zero signal attenuation or mechanical degradation during a rigorous 30-min high-speed fatigue test. Ultimately, this study provides strong evidence of the continuous operational stability of collaborative PEEH in dynamic environments, offering a highly promising hardware solution for battery-free IoT networks.

DECLARATIONS

Authors' contributions

Paper writing and experimental data analysis: Yan, Y.
Core idea, data analysis, and Supervision: Xia, W.; Wang, L.
Normal analyses: Pan, H.; Zhang, X.
Editing and supervision: Wang, Y.; Wang, X.; Yang, R.

Availability of data and materials

Relevant supporting results are provided in the Supplementary Materials. Additional raw data validating the study findings can be obtained from the corresponding author via reasonable requests.

AI and AI-assisted tools statement

Not applicable.

Financial support and sponsorship

This work was supported by the National Key R&D Program of China (2023YFB3208400).

Conflicts of interest

All authors declared that there are no conflicts of interest.

Ethical approval and consent to participate

Not applicable.

Consent for publication

Not applicable.

Copyright

Supplementary Materials

Supplementary Materials

REFERENCES

1. Oztoprak, A.; Hassanpour, R.; Ozkan, A.; Oztoprak, K. Security challenges, mitigation strategies, and future trends in wireless sensor networks: a review. *ACM. Comput. Surv.* **2024**, *57*, 1-29. DOI
2. Karunanithy, K.; Velusamy, B. Cluster-tree based energy efficient data gathering protocol for industrial automation using WSNs and IoT. *J. Ind. Inf. Integr.* **2020**, *19*, 100156. DOI
3. Zhao, X.; Askari, H.; Chen, J. Nanogenerators for smart cities in the era of 5G and Internet of Things. *Joule* **2021**, *5*, 1391-431. DOI
4. Lai, Z.; Xu, J.; Bowen, C. R.; Zhou, S. Self-powered and self-sensing devices based on human motion. *Joule* **2022**, *6*, 1501-65. DOI
5. Lee, D. G.; Shin, J.; Kim, H. S.; et al. Autonomous resonance-tuning mechanism for environmental adaptive energy harvesting. *Adv. Sci.* **2022**, *10*, 2205179. DOI
6. Su, E.; Xu, S.; Wang, Z.; et al. Buoyancy-gravity optimized triboelectric nanogenerators via conductive 3D printing for robust wave energy harvesting. *Mater. Sci. Eng. R. Rep.* **2025**, *164*, 100953. DOI
7. Venkatesan, H. M.; Woo, I.; Yoon, J. U.; Gajula, P.; Arun, A. P.; Bae, J. W. Unveiling the latent potential: Ni/$CoFe_2O_4$-loaded electrospun PVDF hybrid composite-based triboelectric nanogenerator for mechanical energy harvesting applications. *Adv. Compos. Hybrid. Mater.* **2025**, *8*, 221. DOI

8. Lin, Z.; Hong, J.; Huang, C.; et al. A strong, tough, and high-efficiency hydrogel thermocell for thermal energy harvesting. *Nano. Energy*. **2025**, *138*, 110878. DOI
9. Aftab, S.; Goud, B. S.; Ali, Z.; et al. Advancements in nanomaterials for solar energy harvesting: challenges, innovations, and future prospects. *Chem. Eng. J.* **2025**, *516*, 164224. DOI
10. Qi, N.; Yin, Y.; Dai, K.; Wu, C.; Wang, X.; You, Z. Comprehensive optimized hybrid energy storage system for long-life solar-powered wireless sensor network nodes. *Appl. Energy*. **2021**, *290*, 116780. DOI
11. Li , Wang C, Cui X, Chen D, Fei C, Yang Y. Recent progress and development of interface integrated circuits for piezoelectric energy harvesting. *Nano. Energy*. **2022**, *94*, 106938. DOI
12. Shang, C.; Chen, Y.; Dai, Z.; et al. Nanotechnology-enabled devices for ocean Internet of Things. *EcoMat* **2025**, *7*, e70003. DOI
13. Gao, X.; Huang, M.; Zou, G.; Li, X.; Wang, Y. Self-powered vibration sensor based on the coupling of dual-mode triboelectric nanogenerator and non-contact electromagnetic generator. *Nano. Energy*. **2023**, *111*, 108356. DOI
14. Huang, S.; Zhao, X.; Hao, C.; et al. Multifunctional PVDF/CeO_2@PDA nanofiber textiles with piezoelectric and piezo-phototronic properties for self-powered piezoelectric sensor and photodetector. *Chem. Eng. J.* **2024**, *482*, 148950. DOI
15. He, S.; Dai, J.; Wan, D.; et al. Biomimetic bimodal haptic perception using triboelectric effect. *Sci. Adv*. **2024**, *10*, eado6793. DOI PubMed PMC
16. Lu, J.; Chen, X.; Ding, X.; et al. High instantaneous response quartz crystal microbalance humidity sensor for respiratory droplet detection. *Chem. Eng. J.* **2025**, *510*, 161366. DOI
17. Guan, X.; Chen, H.; Xia, H.; Fu, Y.; Yao, J.; Ni, Q. Flexible energy harvester based on aligned PZT/SMPU nanofibers and shape memory effect for curved sensors. *Compos. Part. B. Eng.* **2020**, *197*, 108169. DOI
18. Xia, P.; Sun, H.; Xu, S.; et al. Luminescent solar concentrators with dual functions of photovoltaic and piezoelectric properties for wireless self-powered speed measurement. *Adv. Energy. Mater.* **2023**, *13*, 2301332. DOI
19. Kang, M.; Yum, H. Y.; Kim, H. T.; et al. Self-powered electrical bandage based on body-coupled energy harvesting. *Adv. Mater*. **2024**, *36*, 2402491. DOI
20. Niu, H.; Li, H.; Li, Y.; et al. Cocklebur-inspired "branch-seed-spininess" 3D hierarchical structure bionic electronic skin for intelligent perception. *Nano. Energy*. **2023**, *107*, 108144. DOI
21. Kou, Z.; Zhang, C.; Yu, B.; Chen, H.; Liu, Z.; Lu, W. Wearable all-fabric hybrid energy harvester to simultaneously harvest radiofrequency and triboelectric energy. *Adv. Sci.* **2024**, *11*, 2309050. DOI PubMed PMC
22. Yang, E.; Xu, Z.; Chur, L. K.; et al. Nanofibrous smart fabrics from twisted yarns of electrospun piezopolymer. *ACS. Appl. Mater. Interfaces*. **2017**, *9*, 24220-9. DOI
23. Ham, S. S.; Lee, G.; Hyeon, D. Y.; et al. Kinetic motion sensors based on flexible and lead-free hybrid piezoelectric composite energy harvesters with nanowires-embedded electrodes for detecting articular movements. *Compos. Part. B. Eng.* **2021**, *212*, 108705. DOI
24. Shrestha, K.; Maharjan, P.; Bhatta, T.; et al. A high-performance rotational energy harvester integrated with artificial intelligence-powered triboelectric sensors for wireless environmental monitoring system. *Adv. Eng. Mater*. **2022**, *24*, 2200286. DOI
25. Rani, G. M.; Kim, H.; Pammi, S. V. N.; Umapathi, R.; Huh, Y. S. Next-generation flexible and wearable triboelectric nanogenerator based on PVDF-HFP@GCN composite for mechanical energy scavenging and sleep pattern detection. *Adv. Funct. Mater*. **2025**, *36*, e19594. DOI
26. Wang, F.; Wang, Z.; Zhou, Y.; et al. Windmill-inspired hybridized triboelectric nanogenerators integrated with power management circuit for harvesting wind and acoustic energy. *Nano. Energy*. **2020**, *78*, 105244. DOI
27. Gao, S.; Luo, X.; Wei, H.; Wang, R.; Chen, X.; Zhang, J. Wind-driven suspended triboelectric-electromagnetic hybrid generator with vibration elimination for environmental monitoring in the high-voltage power transmission line. *Nano. Energy*. **2024**, *128*, 109831. DOI
28. Su, B.; Guo, T.; Alam, M. M. A review of wind energy harvesting technology: civil engineering resource, theory, optimization, and application. *Appl. Energy*. **2025**, *389*, 125771. DOI
29. Lu, P.; Pang, H.; Ren, J.; et al. Swing-structured triboelectric-electromagnetic hybridized nanogenerator for breeze wind energy harvesting. *Adv. Mater. Technol.* **2021**, *6*, 2100496. DOI
30. Tang, M.; Cao, H.; Kong, L.; et al. A hybrid kinetic energy harvester for applications in electric driverless buses. *Int. J. Mech. Sci.* **2022**, *223*, 107317. DOI
31. Hu, G.; Yi, Z.; Lu, L.; et al. Self-powered 5G NB-IoT system for remote monitoring applications. *Nano. Energy*. **2021**, *87*, 106140. DOI
32. Wang, L.; Fei, Z.; Duan, C.; et al. Self-sustained and self-wakeup wireless vibration sensors by electromagnetic-piezoelectric-triboelectric hybrid energy harvesting. *Appl. Energy*. **2024**, *355*, 122207. DOI
33. Wang, L.; He, T.; Zhang, Z.; et al. Self-sustained autonomous wireless sensing based on a hybridized TENG and PEG vibration mechanism. *Nano. Energy*. **2021**, *80*, 105555. DOI
34. Wang, L.; Fei, Z.; Wu, Z.; et al. Wearable bending wireless sensing with autonomous wake-up by piezoelectric and triboelectric hybrid nanogenerator. *Nano. Energy*. **2023**, *112*, 108504. DOI

35. Arrigoni, A.; Brambilla, L.; Bertarelli, C.; Serra, G.; Tommasini, M.; Castiglioni, C. P(VDF-TrFE) nanofibers: structure of the ferroelectric and paraelectric phases through IR and Raman spectroscopies. *RSC. Adv.* **2020**, *10*, 37779-96. DOI PubMed PMC
36. Yang, Q.; Shi, Z.; Ma, D.; He, Y.; Wang, J. Flexible $PbTiO_3$-nanowires/ P(VDF-TrFE) composite films and their dielectric, ferroelectric and pyroelectric properties. *Ceram. Int.* **2018**, *44*, 14850-6. DOI
37. Jang, H.; Kim, G. H.; Jeon, D. W.; et al. Long-lasting, steady and enhanced energy harvesting by inserting a conductive layer into the piezoelectric polymer. *Adv. Funct. Mater.* **2024**, *35*, 2415501. DOI
38. Li, Q.; Zhou, H.; Wang, C.; Han, L.; Yang, B.; He, L. A piezoelectric and electromagnetic hybrid energy harvester based on two-stage magnetic coupling. *Mech. Syst. Signal. Proc.* **2024**, *219*, 111601. DOI
39. Cao, H.; Pan, H.; Li, H.; et al. A rotational wind energy harvester based on the centrifugal mechanism for self-powered sensing. *Sustain. Mater. Technol.* **2025**, *46*, e01718. DOI
40. Rui, X.; Li, H.; Han, X.; Zhang, L.; Zhang, Y.; Zeng, Z. A piezoelectric-triboelectric-electromagnetic tri-hybrid energy harvester with dual-frequency-up-conversion mechanism for ultralow-frequency rotational motion. *Sustain. Energy. Technol. Assess.* **2024**, *68*, 103859. DOI
41. Lin, Z.; Ke, J.; Yu, B.; Xia, G.; Cai, M. Improved rotation-excited energy harvester based on adaptive centrifugal force weakening mechanism. *Mechan. Syst. Signal. Proc.* **2025**, *241*, 113474. DOI
42. Fang, S.; Chen, K.; Lai, Z.; Zhou, S.; Liao, W. Analysis and experiment of auxetic centrifugal softening impact energy harvesting from ultra-low-frequency rotational excitations. *Appl. Energy.* **2023**, *331*, 120355. DOI
43. Li, C.; Pang, W.; Li, Z.; et al. Droplet-piezoelectric nanogenerators for simultaneous harvesting of droplet electrostatic and mechanical energy. *Chem. Eng. J.* **2025**, *518*, 164565. DOI
44. Wu, Y.; Zhang, Z.; Wang, J.; et al. An indirectly excited piezoelectric rotational energy harvester exploiting a flexible diaphragm for magnetic coupling. *Renew. Energy.* **2025**, *253*, 123656. DOI
45. Muscalu, G.; Firtat, B.; Anghelescu, A.; et al. Piezoelectric MEMS energy harvester for low-power applications. *Electronics* **2024**, *13*, 2087. DOI
46. Li, Z.; Han, G.; Miao, Z.; Zhu, J.; He, L. A piezoelectric energy harvester for multiple natural environments. *Sustain. Energy. Technol. Assess.* **2025**, *75*, 104236. DOI
47. Xu, W.; Liu, H.; Dong, W.; Zhao, X.; Wang, Y. Study on a magnetostrictive rotating energy harvester utilizing centrifugal frequency modulation via a reversed exponentially tapered primary beam and multi-branch beam. *Smart. Mater. Struct.* **2025**, *34*, 125009. DOI